

© 2019 IEEE. Personal use of this material is permitted. Permission from IEEE must be obtained for all other uses, in any current or future media, including reprinting/republishing this material for advertising or promotional purposes, creating new collective works, for resale or redistribution to servers or lists, or reuse of any copyrighted component of this work in other works.

arXiv:1802.06512v2 [cs.IT] 15 Sep 2019

Asymmetric Modulation Design for Wireless Information and Power Transfer with Nonlinear Energy Harvesting

Ekaterina Bayguzina and Bruno Clerckx

Abstract—Far-field wireless power transfer (WPT) and simultaneous wireless information and power transfer (SWIPT) have become increasingly important in radio frequency (RF) and communication communities recently. The problem of modulation design for SWIPT has however been scarcely addressed. In this paper, a modulation scheme based on asymmetric phase-shift keying (PSK) is considered, which improves the SWIPT rate-energy trade-off region significantly. The nonlinear rectifier model, which accurately models the energy harvester, is adopted for evaluating the output direct current (DC) power at the receiver. The harvested DC power is maximized under an average power constraint at the transmitter and a constraint on the rate of information transmitted via a multi-carrier signal over a flat fading channel. As a consequence of the rectifier nonlinearity, this work highlights that asymmetric PSK modulation provides benefits over conventional symmetric PSK modulation in SWIPT and opens the door to systematic modulation design tailored for SWIPT.

Index Terms—Wireless information and power transfer, modulation, nonlinearity, energy harvesting, rectenna.

I. INTRODUCTION

Radio frequency (RF) wireless power transfer (WPT) has become more important in recent years with the advent of mainly battery free wireless sensor networks (WSN) and Internet of Things (IoT). At the same time, new wireless communications systems enabling simultaneous wireless information and power transfer (SWIPT) are widely investigated in the research community [2]. For the purpose of SWIPT, RF-based WPT is particularly relevant, due to the common use of RF signals in communications, as well as the omnipresence of various radioelectric waves in the ambient environment [3], [4]. Moreover, WPT via radio waves is able to cover longer range as opposed to near-field WPT via inductive coupling or magnetic resonant coupling [5], [6]. With the unification of wireless power and wireless information transfer (WIT), many opportunities arise, such as ubiquitous power accessibility, “green” self-sustainable operation, battery free (or reduced-size) lower cost devices, and true mobility with no wires required to deploy a network [7]. The integration of wireless power and wireless communications brings new

challenges and opportunities, and calls for a paradigm shift in wireless network design. As a result, numerous new research problems need to be addressed that cover a wide range of disciplines including communication theory, information theory, circuit theory, RF design, signal processing, protocol design, optimization, prototyping, and experimentation.

Of particular interest to any communication system is the notion of modulation. Efficient modulations have been designed for several decades to maximize spectral efficiencies and minimize error probability of communication systems [8]. However, with the emerging SWIPT communication paradigm, modulation needs to be re-designed and re-thought. Indeed, while modulation affects the spectral efficiency of the information transfer, it also influences the amount of DC power that can be harvested. This motivates the central question of this work: How to design efficient modulation for SWIPT?

The effect of various conventional communication modulation schemes on the energy conversion efficiency (ECE) as compared to continuous wave (CW) transmission has been considered by the RF community [9]–[12]. In particular, the ECE has been shown to be dependant on various conditions, such as modulation type, input power, and rectifier circuit parameters. In [9], FSK modulated signals were shown to be detrimental in terms of harvested power due to the mixing operation of the diode-based rectifier. In [10], phase and amplitude variations introduced by QPSK and 16QAM were demonstrated to decrease the ECE as compared to the CW. However, in [11], it was established that although the energy harvester (EH) performance is degraded with symmetric modulated signals such as QPSK and 16QAM at high input powers, these modulation schemes improve the ECE at low input powers significantly. In [12], it was shown that the ECE, achieved via multitone and modulated signals, depends on the circuit optimization, mainly on the matching network and the load. Accordingly, a signal with a time-varying envelope can enhance the ECE for a certain range of load values and input power levels in relation to a CW signal with the same average power.

However, modulation schemes designed specifically for the purpose of SWIPT have scarcely been addressed [13]–[15]. In particular, modulation for SWIPT was performed by varying the peak-to-average-power ratio (PAPR) of a multisine signal in [13]; biased ASK was proposed in [14]; and the symbol probabilities of finite rectangular/square constellations were optimized in [15]. Moreover, most of the existing results in the diverse literature on SWIPT are based on the linear model

The authors are with the Department of Electrical and Electronic Engineering, Imperial College London, London SW7 2AZ, U.K. (e-mail: ekaterina.bayguzina08@imperial.ac.uk; b.clerckx@imperial.ac.uk).

This paper was presented in part at the IEEE 19th International Workshop on Signal Processing Advances in Wireless Communications, Kalamata, Greece, June 2018 [1]. This work was supported in part by the EPSRC of the UK, under grants EP/K502856/1, EP/L504786/1 and EP/P003885/1.

Manuscript version 20 August 2019.

of the EH [15]–[21]. Yet, the linear EH model is limited in terms of accuracy, and efforts have recently been devoted to WPT and SWIPT design under nonlinear EH modelling [22]–[28]. Remarkably, systematic waveform design exploiting the EH nonlinearity allows to achieve a higher ECE (and overall end-to-end power transfer efficiency) in a practical rectenna circuit with the use of multiple sinewaves [22], [29]–[32].

Leveraging [22], SWIPT signal design accounting for the rectifier nonlinearity was studied in [23]. It was concluded in [23] that the rectifier nonlinearity radically changes the design of SWIPT. Indeed “it favours a different waveform, modulation, input distribution and transceiver architecture as well as a different use of the RF spectrum. Exploiting the rectifier nonlinearity in the SWIPT design also makes a more efficient use of the resources by enabling enlarged rate-energy regions compared to those obtained by ignoring the nonlinearity in the system design.” Motivated by those observations, the optimal input distribution of SWIPT subject to nonlinear power constraints was studied in [33], [34]. Remarkably, it was shown that the capacity of an additive white Gaussian noise (AWGN) channel under transmit average power and nonlinear delivered power constraints is the same as the capacity of an AWGN channel under an average power constraint. In other words, the capacity of an AWGN channel is independent of the value of the delivered power constraint. The capacity can be arbitrarily approached by using time sharing between distributions with high amount of information, e.g. circularly symmetric complex Gaussian (CSCG) inputs, and distributions with high amount of power reminiscent of flash signaling exhibiting a low probability of high amplitude signals.

In this paper, we investigate modulation for SWIPT considering the accurate nonlinear model for the EH at the receiver and flat fading environment. We study modulation of information symbols onto the multi-carrier energy-carrying waveform, resulting in a unified SWIPT waveform. Uniquely, we introduce asymmetric PSK modulation and show its suitability for SWIPT. In the following, we summarize the contributions of this paper.

- The nonlinear model of the rectifier is extended in order to account for the randomness in phases of carriers. In particular, we choose the phases to be independent and identically distributed (i.i.d.) random variables with uniform distribution. We show through analytical derivation that the scaling of the harvested energy with the number of carriers exhibits increasing losses as the phase range increases, degrading the benefit of using a multi-carrier signal. However, departing from the in-phase condition for maximum power transfer opens up a possibility of transmitting information with symbols distributed uniformly over a non-zero phase range.
- We formulate the asymmetric *M*PSK modulation scheme and obtain a metric for the harvested energy given mass probabilities of the input symbols. We then derive the achievable information rate for a flat fading channel, and consequently, obtain the optimal input distribution for the proposed modulation scheme maximizing the rate only. Finally, we characterize the SWIPT rate-energy region considering the designed modulation and optimize the

probabilities of the input symbols under rate and energy constraints.

- We conclude the results by providing the complimentary numerical results. We support all the observations with simulations of a practical rectenna circuit. The main observations are that 1) the nonlinear EH model allows to optimize the probabilities of symbols for symmetric and asymmetric PSK modulations, enlarging the rate-energy region; 2) asymmetric PSK is advantageous over symmetric PSK in terms of harvested energy, and additionally, it is not too detrimental in terms of information rate, as such phase range can be obtained for a given signal-to-noise ratio (SNR) in order to balance the rate-energy maximization mechanisms; 3) analysis of optimized probabilities of symbols confirms that maximum power transfer is achieved with in-phase multi-carrier transmission, whereas maximum rate corresponds to the optimal input distribution obtained via the Blahut-Arimoto algorithm.

Organization: In Section II, the SWIPT system model is introduced. In Section III, the design of the asymmetric PSK modulation and the optimization of the rate-energy region is studied. In Section IV, the simulation results are presented. Finally, Section V concludes the paper.

Notation: Throughout this paper, the operators $\mathcal{E}\{\cdot\}$ and $\mathbb{E}\{\cdot\}$ refer to the average over time and the expectation over statistical randomness, respectively. Upper case letters stand for random variables and random processes, except for in relation to circuit notations. The probability density (mass) function of a continuous (discrete) random variable X is denoted by $p_X(x)$, and the probability of an event is denoted by $\Pr(\cdot)$. $\Re\{\cdot\}$ and $\Im\{\cdot\}$ indicate real and imaginary operators, respectively. The standard circularly symmetric complex Gaussian distribution is denoted by $\mathcal{CN}(0, 1)$. $\text{Var}\{\cdot\}$ refers to the variance of a random variable. $U[-a, a]$ denotes the uniform distribution over the interval $[-a, a]$. The convolution operator is denoted by $*$.

II. SWIPT SYSTEM MODEL

We study the system model illustrated in Fig. 1, in which a single-input single-output (SISO) point-to-point SWIPT is considered and the receiver is assumed to be able to simultaneously decode information and harvest energy. We consider a multi-carrier/band transmission (with single-carrier being a special case) consisting of N orthogonal subbands where the n th subband has carrier frequency f_n and equal bandwidth B_s , $n = 0, \dots, N - 1$. The carrier frequencies are evenly spaced such that $f_n = f_0 + n\Delta_f$ with Δ_f denoting the inter-carrier frequency spacing (with $B_s \leq \Delta_f$). The channel, over which the signal is transmitted, is assumed to be flat fading (when $(N - 1)\Delta_f$ is much smaller than the channel coherence bandwidth) and is subject to AWGN, originating from the receiver antenna and the RF-to-baseband processing at the information decoder. Throughout the paper, we assume that the power of the processing noise Z_n is much larger than the power of the antenna noise W_n and that the effect of the antenna noise is negligible for energy harvesting purposes [2].

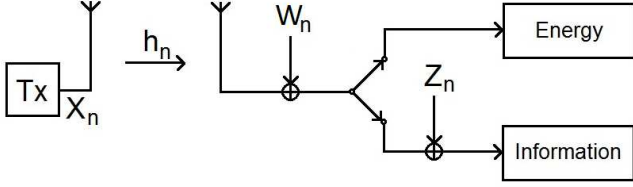


Fig. 1. System model with the receiver simultaneously decoding information and harvesting energy.

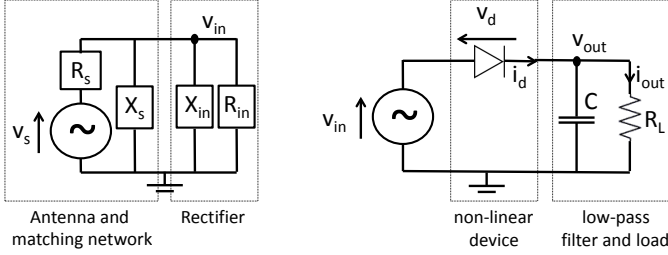


Fig. 2. Antenna equivalent circuit (left) and a single series diode rectifier (right).

A. Transceiver Design

Considering a multi-carrier transmission, the channel input is given as

$$x(t) = \Re \left\{ \sum_{n=0}^{N-1} X_n e^{j2\pi f_n t} \right\} \quad (1)$$

with $X_n = S_n e^{j\Phi_n}$, where S_n and Φ_n refer to the amplitude and phase of the n^{th} carrier at frequency f_n . The transmitter is subject to a transmit power constraint $\mathbb{E} \left\{ |X_n|^2 \right\} \leq P$.

The transmitted signal $x(t)$ propagates through a multipath channel. The received signal at the receiver is modelled as

$$y(t) = \Re \left\{ \sum_{n=0}^{N-1} h_n X_n e^{j2\pi f_n t} \right\}, \quad (2)$$

where h_n is the channel frequency response at frequency f_n .

B. Antenna Equivalent Circuit Model

The antenna model reflects the power transfer from the antenna to the rectifier through the matching network. As illustrated in Fig. 2 (left), a lossless antenna can be modelled as a voltage source $v_s(t)$ followed by a series resistance R_s and a parallel reactance X_s . The rectifier is modelled as a resistance R_{in} in parallel with a reactance X_{in} . Assuming perfect matching ($R_{in} = R_s$, $X_{in} = -X_s$), all the available RF power $P_{in,av}$ is transferred to the rectifier and absorbed by R_{in} , so that $P_{in,av} = \mathbb{E} \left\{ \mathcal{E} \left\{ |v_{in}(t)|^2 \right\} \right\} / R_s$. Since $P_{in,av} = \mathbb{E} \left\{ \mathcal{E} \left\{ |y(t)|^2 \right\} \right\}$, $v_{in}(t) = y(t) \sqrt{R_s}$ and $v_s(t)$ can be formed as

$$v_s(t) = 2y(t) \sqrt{R_s}. \quad (3)$$

C. Rectifier and Diode Nonlinear Model

Consider a rectifier composed of a single series diode followed by a low-pass filter with a load as in Fig. 2 (right). Denote the voltage drop across the diode as $v_d(t) = v_{in}(t) - v_{out}(t)$ where $v_{in}(t)$ is the input voltage to the diode and $v_{out}(t)$ is the output voltage across the load resistor. A tractable behavioural diode model is obtained by Taylor series expansion of the diode characteristic equation $i_d(t) = i_s \left(e^{\frac{v_d(t)}{n v_t}} - 1 \right)$ (with i_s the reverse bias saturation current, v_t the thermal voltage, and n the diode ideality factor) around a quiescent operating point $v_d = a$, namely

$$i_d(t) = \sum_{i=0}^{\infty} k_i (v_d(t) - a)^i, \quad (4)$$

where $k_0 = i_s \left(e^{\frac{a}{n v_t}} - 1 \right)$ and $k_i = i_s \frac{e^{\frac{a}{n v_t}}}{i! (n v_t)^i}$, $i = 1, \dots, \infty$ [22].

Assume a steady-state response and an ideal low pass filter, such that $v_{out}(t)$ is at a constant DC level. Choosing $a = \mathbb{E} \left\{ \mathcal{E} \left\{ v_d(t) \right\} \right\} = -v_{out}$, (4) can be simplified as

$$i_d(t) = \sum_{i=0}^{\infty} k_i v_{in}(t)^i = \sum_{i=0}^{\infty} k_i R_s^{i/2} y(t)^i. \quad (5)$$

In order to make the model and the modulation design more tractable, we truncate (5) to the fourth order that is sufficient to retain the fundamental nonlinear behaviour of the diode [22], [35]. After truncation and taking the average over time and the expectation over statistical randomness, the DC component of $i_d(t)$ is approximated as $i_{out} \approx k_0 + z_{DC}$ where

$$z_{DC} = k_2 R_s \mathbb{E} \left\{ \mathcal{E} \left\{ y(t)^2 \right\} \right\} + k_4 R_s^2 \mathbb{E} \left\{ \mathcal{E} \left\{ y(t)^4 \right\} \right\}. \quad (6)$$

In (6), the coefficients $k_2 = 0.0034$ and $k_4 = 0.3829$ are calculated for a typical zero-bias Schottky diode with $i_s = 5 \mu\text{A}$ and $n = 1.05$, and $v_t = 25.86 \text{mV}$. This model has been validated for the design of multisine waveform in [22], [29], [30] using circuit simulators with various rectifier topologies and input power and in [30], [31] through prototyping and experimentation. It has also been validated using circuit simulator for modulated single-carrier [34] and modulated multi-carrier waveform with Gaussian input [23].

III. MODULATION DESIGN FOR SWIPT

Considering a flat fading channel with gains given as $h_n = 1$ for $n = 0, \dots, N-1$, in the following, we first study the scaling of the harvested power at the receiver with respect to the number of carriers in Section III.A, as well as the variation in the phase range of the transmitted signal. This analysis demonstrates how the random phase affects the harvested power by reducing the gains of the multi-carrier transmission. Moreover it gives an insight into how the adverse effects of the phase variation can be mitigated by efficient modulation design and why SWIPT modulations differ from conventional communication modulations. Next, in Section III.B, we consider the MPSK modulation design for SWIPT purposes. In Section III.C, we study the ultimate information-theoretic achievable rate for the considered MPSK modulation. Finally, in Section III.D, we consider optimization of the harvested power under

an average power constraint and a received information rate constraint.

A. Scaling Law for Uniformly Distributed Random Phase

An analytical expression for z_{DC} in (6) is now derived using the multi-carrier signal with uniform power allocation across the carriers with $S_n = s = \sqrt{\frac{2P}{N}}$, $n = 0, \dots, N-1$ and uniformly distributed random phases. Choosing the phases of different carrier frequencies f_n , $n = 0, \dots, N-1$ to be i.i.d. with $\Phi_n \sim U[-\delta, \delta]$, $n = 0, \dots, N-1$, $\delta \leq \pi$, for a flat fading channel, the received signal $y(t)$ is given by

$$y(t) = \sqrt{\frac{2P}{N}} \sum_{n=0}^{N-1} \cos(2\pi f_n t + \Phi_n). \quad (7)$$

The second and fourth order terms in z_{DC} are further simplified as follows. By taking the time average and expectation over the randomness of the signal, we have:

$$\mathbb{E}\{\mathcal{E}\{y(t)^2\}\} = P, \quad (8)$$

$$\mathbb{E}\{\mathcal{E}\{y(t)^4\}\} = \frac{3P^2}{2N^2} \sum_{\substack{n_0, n_1, n_2, n_3 \\ n_0 + n_1 = n_2 + n_3}} \mathbb{E}\{\cos(\Phi_{n_0} + \Phi_{n_1} - \Phi_{n_2} - \Phi_{n_3})\}. \quad (9)$$

Note that in (8) and (9), we have neglected the noise power. Else, we assume that the average power constraint at the transmitter is satisfied with equality. For details on the derivation of (8) and (9), refer to Section III.C in [22]¹.

Denoting the random term in (9) as

$$\Theta = \Phi_{n_0} + \Phi_{n_1} - \Phi_{n_2} - \Phi_{n_3}, \quad (10)$$

the resultant probability density function (p.d.f.) of Θ is obtained by convolving four uniform distributions $\Phi_{n_i} \sim U[-\delta, \delta]$, $i = 0, \dots, 3$. The exact distribution of Θ can also be approximated with a normal distribution. In [36], it is shown that the sum of I i.i.d. and uniformly distributed random variables converges to the normal distribution extremely fast. Accordingly, we approximate the distribution of Θ in (10) by a normal distribution $\mathcal{N}(\sum_{i=0}^3 \mathbb{E}\{\Phi_{n_i}\}, \sum_{i=0}^3 \text{Var}\{\Phi_{n_i}\})$ with

$$\mathbb{E}\{\Phi_{n_i}\} = 0, \quad (11)$$

$$\text{Var}\{\Phi_{n_i}\} = \frac{\delta^2}{3}. \quad (12)$$

The distribution of Θ is thus approximated as $\Theta \sim \mathcal{N}(0, \frac{4\delta^2}{3})$. The difference between the exact distribution and the normal approximation for $\delta = \pi/3$ is shown in Fig. 3.

Next, the expected mean of the random variable $\cos(\Theta)$ is obtained as follows:

$$\mathbb{E}\{\cos(\Theta)\} = \Re\{\mathbb{E}\{e^{j\Theta}\}\} = e^{-\frac{2\delta^2}{3}}. \quad (13)$$

¹Equations (8) and (9) can be obtained, respectively, from equations (12) and (14) of [22] by substituting in the latter $A_n = h_n = 1$, $s_n = s = \sqrt{\frac{2P}{N}}$ and $\psi_n = \Phi_n$ for $n = 0, \dots, N-1$, for a single transmit antenna.

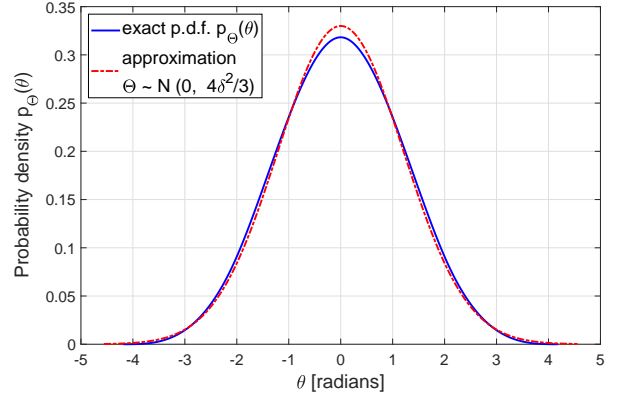


Fig. 3. The exact and normal approximation of the p.d.f. of Θ with $\delta = \pi/3$.

Finally, noting that there are $N(2N^2 + 1)/3$ terms in the sum of (9), the scaling law for z_{DC} for the signal $y(t)$ in (7) is obtained as

$$z_{DC}(\delta) \simeq k_2 R_s P + k_4 R_s^2 \frac{(2N^2 + 1)}{2N} P^2 e^{-\frac{2\delta^2}{3}}. \quad (14)$$

It is observed that the harvested power given by the z_{DC} metric increases with N but decreases with δ . The rate of scaling of z_{DC} with N is diminished with enlarging the phase range, until it becomes nearly flat for $\Phi_n \sim U[-\pi, \pi]$. Moreover, the case of $\delta = 0$ is equivalent to the scaling exhibited by the deterministic multisine signal in a frequency-flat channel in [22], whereas the case of $\delta = \pi$ leads to a scaling behaviour similar to the multi-carrier signal modulated with CSCG inputs in [23]. Thus, departing from the in-phase condition for maximum power transfer makes it possible to simultaneously transfer information with a phase-modulated multi-carrier signal.

Remark 1: While (14) is obtained as a result of the truncation of (5) to the fourth order and the Gaussian approximation of the distribution of Θ in (10), the observations above still hold if these approximations are removed. Firstly, considering as an example a typical input power of -20 dBm at the EH receiver with the diode parameters from Section II.C and $N = 8$, the ratio of the second order term to the fourth order term in (14) can be obtained as $\approx \frac{k_2 e^{-\frac{2\delta^2}{3}}}{k_4 R_s^2 N P} = 2.2 e^{-\frac{2\delta^2}{3}}$. Therefore, the second order term is dominating over the fourth (with the contribution of the fourth order term decreasing with larger δ), and truncation to the fourth order is sufficient to accurately capture the diode nonlinear behaviour in the low power regime. Secondly, the speed of the convergence of the result of the convolution of the identical uniform distributions of Φ_{n_i} in the argument of $\cos(\cdot)$ to the normal distribution is extremely fast [36] and increasing with the number of Φ_{n_i} . Therefore, if (5) is truncated to a higher order, the difference due to the Gaussian approximation can be attributed at most to the approximation of the p.d.f. $p_\Theta(\theta)$ in the fourth order term (which can be considered a minimal difference, as shown in Fig. 3) rather than in the higher order terms.

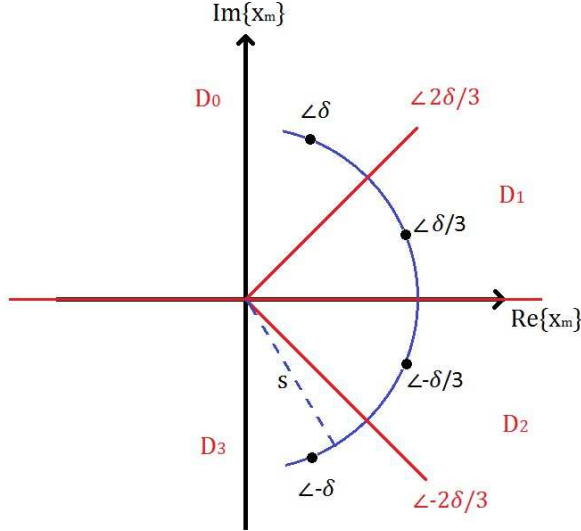


Fig. 4. Asymmetric 4PSK constellation with $\delta = \pi/3$. MAP decision boundaries are shown by red lines.

B. Asymmetric MPSK Modulation Design for SWIPT

The scaling law for z_{DC} (14) motivates the use of modulation schemes, in which symbols are distributed in a limited phase range. Accordingly, this allows to obtain higher gains in harvested power.

Motivated by the WPT observations in Section III.A, for asymmetric MPSK modulation, the symbols are given as

$$X_n \in \left\{ x_m = s e^{\pm j(2m+1)\delta/(M-1)}, m = 0, 1, \dots, \frac{M}{2} - 1 : |\delta| < \pi \right\}, n = 0, \dots, N - 1. \quad (15)$$

Note that choosing $\delta = \pi$ yields the standard symmetric MPSK modulation:

$$X_n \in \left\{ x_m = s e^{\pm j(m+1)\pi/M}, m = 0, 1, \dots, \frac{M}{2} - 1 : |\delta| = \pi \right\}, n = 0, \dots, N - 1. \quad (16)$$

As an example, an asymmetric 4PSK constellation with $\delta = \pi/3$ is illustrated in Fig. 4, along with the decision regions for maximum a posteriori (MAP) detecting at the receiver side. For details on the relevant MAP decision rule, see Appendix A.

In analogy to obtaining the p.d.f. of Θ in (10) for the case of continuously distributed phase in Section III.A, the probability mass function (p.m.f.) of Θ is found for the case of discretely distributed phase by discrete convolution of the p.m.f.s of Φ_{n_i} . The resultant support of Θ is

$$\text{supp}(\Theta) = \left\{ \theta_k = -4\delta + \frac{2\delta k}{M-1}, k = 0, 1, \dots, 4(M-1) : |\delta| < \pi \right\} \quad (17)$$

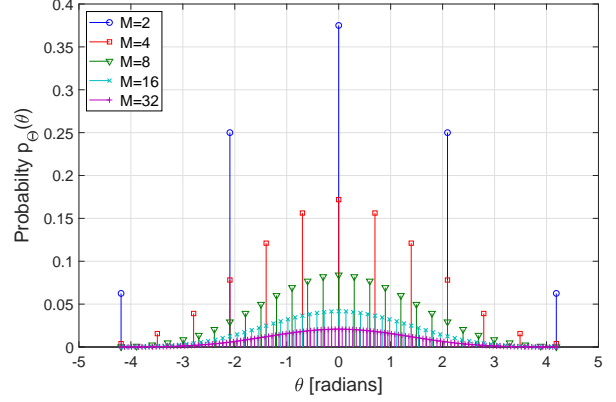


Fig. 5. The p.m.f. of Θ for $\delta = \pi/3$

for the case of asymmetric MPSK in limited phase range and

$$\text{supp}(\Theta) = \left\{ \theta_k = \frac{(-4(M-1) + 2k)\pi}{M}, k = 0, 1, \dots, 4(M-1) : |\delta| = \pi \right\} \quad (18)$$

for the symmetric MPSK. As an illustration for the above, Fig. 5 depicts $p_{\Theta}(\theta)$ for the asymmetric MPSK modulation with $\delta = \pi/3$ with uniform input distribution $p_X(x) = 1/M$ for different values of M .

To account for the discrete distribution of the phases Φ_{n_i} , the scaling law in (14) is modified as follows:

$$z_{DC}(\xi) \simeq k_2 R_s P + k_4 R_s^2 \frac{(2N^2 + 1)}{2N} P^2 \xi, \quad (19)$$

where $\xi = \sum_{k=0}^{4M-4} \cos(\theta_k) \Pr(\Theta = \theta_k)$ gives the expected mean of $\cos(\Theta)$ and replaces that in (13), used earlier for the continuous phase distribution. Note that the received energy is maximized when $\xi = 1$.

For convenience, the random term in (19) is rewritten in vector form as $\xi = \cos(\Theta) \bar{\mathbf{p}}^T$, where $\cos(\Theta) = [\cos(\theta_0) \dots \cos(\theta_{4M-4})]$ and $\bar{\mathbf{p}} = [\Pr(\Theta = \theta_0) \dots \Pr(\Theta = \theta_{4M-4})]$ are the cosine of the support of the random variable Θ in (17)-(18) and the corresponding probabilities obtained as $\bar{\mathbf{p}} = \mathbf{p} * \mathbf{p} * \hat{\mathbf{p}} * \hat{\mathbf{p}}$, respectively. In the latter, $\mathbf{p} = [p_0 \dots p_{M-1}]$ denotes the p.m.f. of the symbols in MPSK constellation using the notation $p_m = \Pr(X = x_m)$ and $\hat{\mathbf{p}} = [p_{M-1} \dots p_0]$ is the version of the vector \mathbf{p} with the flipped order of elements. The flipping is necessary to account for the subtractions of the two random variables Φ_{n_i} in the expression for Θ in (10).

In comparison to deterministically scaling $z_{DC}(\delta)$ in (14), the discrete probabilistic nature of ξ in (19) means that $z_{DC}(\xi)$ not only decreases with increasing the phase range δ , but also depends on the choice of the probability masses of the symbols and may be larger or smaller than in the case of the uniform phase distribution. It is also noted that for a certain δ , equiprobable modulation of a large enough order M will behave similarly to the uniformly distributed phase, and the scaling laws (14) and (19) will also nearly match. As a basis for this, consider the p.d.f. and the p.m.f. of Θ for the same δ in Figs. 3 and 5, respectively. As M grows

large, $\Pr(\Theta = \theta_k) \rightarrow 0 \quad \forall k$, which is characteristic of a p.d.f, meaning that the difference in the discrepant fourth order terms in (14) and (19) fades away.

Given the asymmetric geometry of the constellation as depicted in Fig. 4, the modulation design of MPSK with limited phase range will consist in mainly optimizing the input probability distribution \mathbf{p} for a given δ , determined by the overall objective of achieving certain rate-energy performance. On one hand, from the information-theoretic perspective, this transcribes into choosing asymmetric input p.m.f. that allocates higher probability to the outer symbols than to the inner, in order to achieve lower symbol error probability for detecting information. On the other hand, from the energy transfer perspective, the reverse is preferred, with the asymmetric p.m.f. assigning higher probability to the constellation points with a small phase difference, as deduced from Section III.A, with the deterministic single symbol transmission giving the maximum harvested energy. In any case, a non-uniform input distribution is required to balance the rate and energy maximization goals [15].

Remark 2: Asymmetric geometry of constellation appears in the works on coded modulation design for passive backscatter communication in RFID systems [37]–[39]. In particular, it is shown that constellation with unequal energy per bit in in-phase and quadrature components, such as rectangular 4QAM modulation, allows to maximize the harvested power while improving the spectral efficiency of the backscatter uplink, as compared to commonly used binary modulation. This highlights that the RF energy harvesting mechanism generally favours asymmetry in modulation throughout a range of WPT applications, which differs from modulation design requirements for wireless information only communication systems.

Remark 3: Asymmetry also appeared in the derivation of input distribution for single-carrier SWIPT in [33], [34], because asymmetric inputs are characterized by higher order moments.

C. Information Rate Computations

In this subsection, we aim at maximizing the achievable rate when the transmitter utilizes asymmetric MPSK modulation.

1) *Achievable Information Rate:* Consider a multi-carrier transmission with N carriers over a flat fading deterministic channel, i.e. $h_n = 1$, $n = 0, \dots, N-1$. We aim at maximizing the mutual information $I(\mathbf{X}; \mathbf{Y})$ between the input vector $\mathbf{X} = [X_0 \dots X_{N-1}]$ and the output vector $\mathbf{Y} = [Y_0 \dots Y_{N-1}]$, when the transmitter utilizes asymmetric MPSK modulation (see equation (15)) with $s = \sqrt{\gamma}$, where γ denotes the signal-to-noise ratio (SNR). We assume that different carriers (subchannels) are statistically independent of each other, i.e. $\Pr(\mathbf{Y}|\mathbf{X}) = \prod_{n=0}^{N-1} \Pr(Y_n|X_n)$. Therefore, under this assumption and due to the fact that X_n , $n = 0, \dots, N-1$ are i.i.d., the achievable rate at the receiver is given by

$$I_N \triangleq I(\mathbf{X}; \mathbf{Y}) = NI(X_0; Y_0). \quad (20)$$

Accordingly, in the following, we equivalently focus on maximizing $I(X_0; Y_0)$. For clarity, in the sequel, we omit the

subchannel index. The channel input and output are related through

$$Y = X + Z, \quad (21)$$

where Z is an AWGN distributed as $\mathcal{CN}(0, 1)$.

The capacity of the channel in (21) is obtained by maximizing the following mutual information

$$I(X; Y) = H(Y) - \log_2(\pi e). \quad (22)$$

The output entropy $H(Y) = -\int \log_2(p_Y(y))p_Y(y)dy$ in (22) is computed by using Monte-Carlo or numerical integration [8], where the output p.d.f. $p_Y(y)$ is given as

$$\begin{aligned} p_Y(y) &= \sum_{m=0}^{M-1} p_X(x_m)p_Z(y-x_m) \\ &= \frac{1}{\pi} \sum_{m=0}^{M-1} p_m e^{-|y-\sqrt{\gamma}e^{j\phi_m}|^2}. \end{aligned} \quad (23)$$

2) *Optimal Input Distribution:* For MPSK with limited phase range, the optimal input distribution $p_X(x)$ needs to be derived in order to calculate the capacity.

The conditional p.d.f. of the channel output given the channel input for an M -ary constellation is

$$p_{Y|X}(y|x_m) = \frac{1}{2\pi\sigma^2} e^{-\frac{|y-x_m|^2}{2\sigma^2}}, \quad m = 0, \dots, M-1. \quad (24)$$

Using MAP detector with the detected symbol denoted as \hat{X} , the decision region D_l for $\hat{X} = x_l$ for $l = 0, \dots, M-1$ is given by

$$D_l = \{y = |y|e^{j\phi} : \phi_{L_l} \leq \phi < \phi_{U_l}\}, \quad (25)$$

where ϕ_{L_l} and ϕ_{U_l} denote the lower and the upper border phases of the decision region for a given symbol x_l . The transition probabilities for this discrete memoryless channel are obtained as

$$\begin{aligned} \Pr(\hat{X} = x_l | X = x_m) &= \Pr(\phi_{L_l} \leq \Phi < \phi_{U_l} | X = x_m) \\ &= \int_{\phi_{L_l}}^{\phi_{U_l}} p_{\Phi|x_m}(\phi|x_m) d\phi, \end{aligned} \quad (26)$$

where the conditional phase p.d.f. is derived from (24) as in [40] and is given by

$$\begin{aligned} p_{\Phi|x}(\phi|x_m) &= \frac{1}{2\pi} e^{-\gamma} + \sqrt{\frac{\gamma}{\pi}} \cos(\phi - \phi_m) e^{-\gamma \sin^2(\phi - \phi_m)} \\ &\quad \times \left[1 - Q\left(\sqrt{2\gamma} \cos(\phi - \phi_m)\right) \right]. \end{aligned} \quad (27)$$

For every range of phase, the transition probabilities channel matrix is calculated using (26) and the optimal input distribution can be obtained with the Blahut-Arimoto algorithm [41]–[42].

D. Rate-Energy Region Optimization

We can now define the achievable rate-energy region (or, more accurately, rate-DC current) region as

$$C_{R-I_{DC}}(p_X(x)) \triangleq \left\{ (R, I_{DC}) : R \leq I_N, \right. \\ \left. I_{DC} \leq z_{DC}, \sum_{m=0}^{M-1} p_m = 1 \right\}. \quad (28)$$

In order to identify the rate-energy region, one possible way is to formulate the optimization problem as an energy maximization problem subject to rate constraint over the p.m.f. of input symbols, such as

$$\max_{\{p_m\}} z_{DC} \quad (29)$$

$$\text{subject to } I_N \geq R, \quad (30)$$

$$\sum_{m=0}^{M-1} p_m = 1, \quad (31)$$

where z_{DC} and I_N are given in (19) and (20), respectively. Note that both z_{DC} and I_N are dependent on the phase range δ , number of mass points M , values of mass points $\{p_m\}_{m=0}^{M-1}$ and number of carriers N .

The objective function to be minimized is transformed as $f_0 = -z_{DC}$ and the rate constraint is set as $f_1 = R - I_N \leq 0$. The optimization problem (29)-(31) can then be rewritten as

$$\min_{\mathbf{p}} f_0(\mathbf{p}) \quad (32)$$

$$\text{subject to } f_1(\mathbf{p}) \leq 0, \quad (33)$$

$$\mathbf{1}^T \mathbf{p} - 1 = 0, \quad (34)$$

where \mathbf{p} is the vector representation of $\{p_m\}_{m=0}^{M-1}$.

The rate constraint is convex in \mathbf{p} due to the concavity of the output entropy $H(Y)$ when I_N is evaluated numerically over a restricted domain. However, the objective function is non-convex, as it is in essence a signomial function in the variables $\{p_m\}$ as some coefficients $\cos(\theta_k)$ of the products of powers of $\{p_m\}$ are negative in ξ in (19) (see Appendix B for an example). Because the rate constraint cannot be represented as a posynomial or a signomial, the obtained optimization problem (32)-(34) is not compatible with standard Signomial Geometric Programming (SGP) tools [43]. However, a locally optimal solution can still be obtained efficiently with Sequential Quadratic Programming (SQP) algorithm [44] that is a quasi-Newton method for solving inequality-constrained non-linear programming problems. For details on the gradients of the energy and rate functions as supplied in SQP optimization, see Appendix C.

IV. SIMULATION RESULTS

We first present analytical and numerical results for harvested energy with multi-carrier transmission and uniformly distributed random phases. Next, focussing on the aspect of WIT only, we obtain the optimal input distribution for the proposed asymmetric MPSK modulation and calculate the maximum achievable information rate. We then show

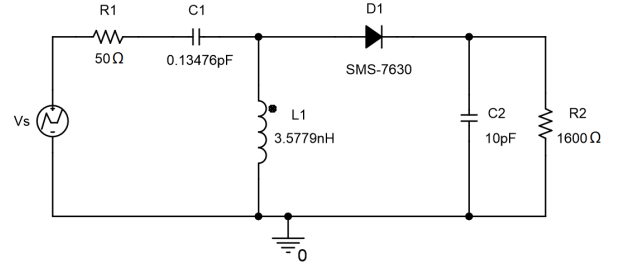


Fig. 6. Rectenna with a single series diode rectifier.

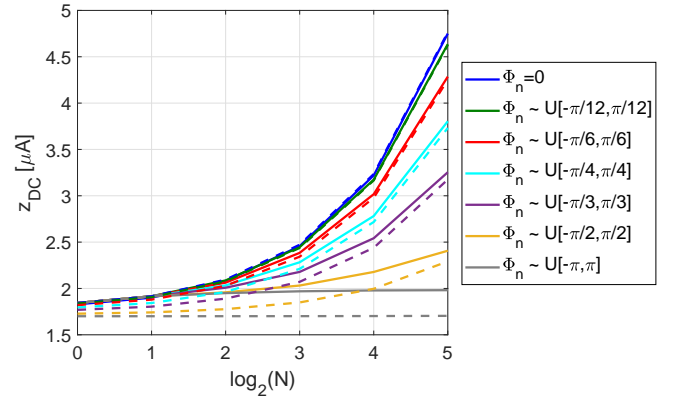


Fig. 7. z_{DC} obtained numerically (solid lines) and with the scaling law (dash lines) as a function of $\log_2(N)$.

optimization results for the rate-energy region with asymmetric MPSK modulation. Finally, we analyse the simulation results for the symbols' p.m.f. optimized for SWIPT and how harvested energy scales with the modulation order M .

All SWIPT observations are confirmed by PSpice simulations of a practical rectenna circuit. The rectenna design (Fig. 6) is optimized for the input signal composed of 4 in-phase carriers centered around 5.18GHz and the available RF power $P_{in,av}$ of -20dBm . The package parasitics of components are ignored. The L-matching network is optimized together with the load resistor, with the objective to maximize the output DC power and minimize impedance mismatch due to a signal of varying instantaneous power.

A. Results for Multi-Carrier Transmission with Uniformly Distributed Random Phase

Fig. 7 represents z_{DC} as a function of the number of carriers N with the phase of each carrier chosen to be i.i.d. distributed as $\Phi_n \sim U[-\delta, \delta]$. The value of z_{DC} is obtained numerically by averaging over several hundred symbol periods using (6). The power P is set as -20dBm and N carriers are centered around 5.18GHz with a frequency gap fixed as $\Delta_f = B/N$ for bandwidth $B = 10\text{MHz}$. The symbol period is set as $T = 1/\Delta_f$. Fig. 7 also illustrates the scaling law in (14) for z_{DC} as a function of the number of carriers N for different values of δ . As it is observed, apart from the small N region, there is a good match between the analytical and the numerical results. This inaccuracy for small values of N can be justified by the following fact. When the carriers

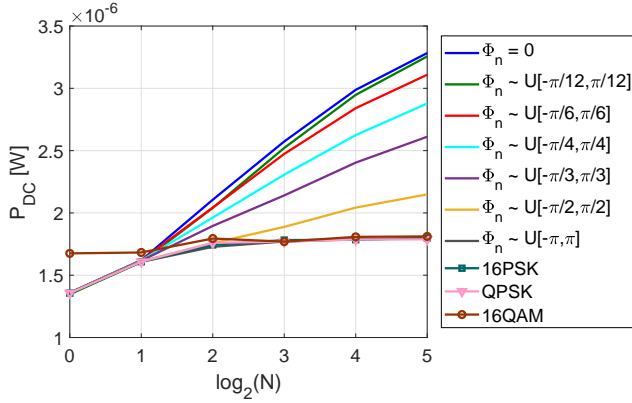


Fig. 8. Average DC power P_{DC} as a function of $\log_2(N)$ for input signals with with i.i.d. uniformly distributed phases.

with the same index $n_i = n_j$ (and, consequently, with the same phase $\Phi_{n_i} = \Phi_{n_j}$) are combined in the summation in (9), they contribute constructively to the channel output. This effect is particularly pronounced for small values of N and is not captured by the analytical model in (14). The small variations in the analytical and the numerical z_{DC} for $\delta = \pi$ are due to the same aforementioned reason.

To validate the scaling laws of Fig. 7, the rectenna circuit of Fig. 6 is simulated by using the input data signals with uniformly distributed random phase. The PSpice simulations results in terms of the DC output power (Fig. 8) confirm the analytical and the numerical results using the z_{DC} metric (Fig. 7). The P_{DC} behaviour naturally has a more saturated form due to the non-optimality of the circuit design for large N (because of the choice of the finite output capacitor and load).

It is verified that, in the nonlinear operating region of the diode at low input power, the circuit is very sensitive to randomness in phase, with the losses due to phase variations increasing with N . On the other hand, amplitude randomness can be beneficial for energy harvesting purposes at low input power, due to high power waveform peaks driving the diode with higher efficiency. As a result, it is observed that 16QAM is slightly better than PSK for small N in accordance with [11], but as N grows, there are less high power peaks for QAM and this benefit of 16QAM over PSK is lost. In addition, it is noted that QPSK and 16PSK modulations with equiprobable signaling perform equivalently to the case of $\Phi_n \sim U[-\pi, \pi]$. This highlights that the constellation size of symmetric MPSK modulation with uniform p.m.f. has no effect on harvested energy, because in such case $\xi = 0$ in the fourth order component of (19) resulting in $z_{DC} \simeq k_2 R_s P$, same as for $\Phi_n \sim U[-\pi, \pi]$.

B. Results for Information Rate with Asymmetric MPSK Modulation

Considering a single WIT channel, in Fig. 9, the mutual information is obtained using (22) for different ranges $[-\delta, \delta]$ of 4PSK constellation with uniform and optimal input distributions, where the latter is computed using the Blahut-Arimoto algorithm [41]–[42] and the channel transition probabilities

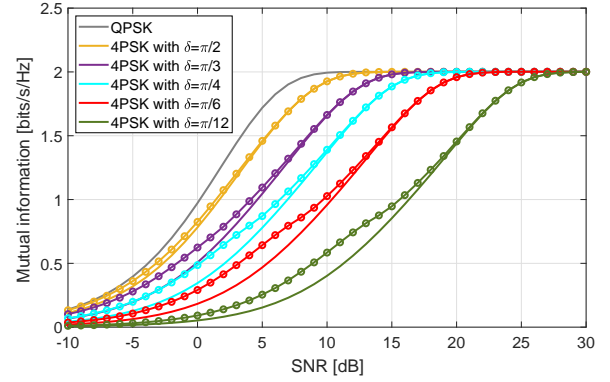


Fig. 9. Mutual information for 4PSK in different ranges $[-\delta, \delta]$ with uniform and optimal input distributions. (Marked lines correspond to $p_X(x)$ optimized with the Blahut-Arimoto algorithm).

given by (26). It is noted that for asymmetric MPSK modulation, the equiprobable input distribution $p_X(x)$ is not optimal anymore and optimizing $p_X(x)$ with the Blahut-Arimoto algorithm further maximizes the mutual information. As an example, for $\delta = \pi/4$ at $\gamma = 10$ dB, the outer symbols have been optimized to probabilities $p_0 = p_3 = 0.327$ and the inner symbols – to probabilities $p_1 = p_2 = 0.173$. It is also noted that the input distribution converges to the uniform distribution at high SNR values. Finally, it is observed that such choice of δ can be made for a given SNR, which does not lead to a large gap between the maximum information rate of the symmetric MPSK modulation and that achievable with the asymmetric MPSK modulation. Moreover, at high SNR values, the rate close to that of the symmetric MPSK modulation is achievable with even small $[-\delta, \delta]$ ranges.

C. Results for Rate-Energy Region with Asymmetric MPSK Modulation

The rate-energy region is obtained by solving the optimization problem (29)–(31) with the help of MATLAB Optimization Toolbox and the choice of SQP for *fmincon* algorithm.

Fig. 10 illustrates the achievable rate-energy region for 4PSK in various phase range limits for a single ($N = 1$) and multiple ($N = 8$) carrier transmission and SNR of 20dB. The total information rate I_N is normalized w.r.t. the bandwidth NB_s . Hence, the x-axis refers to a per-subband rate. The gains due to using optimized modulation and multi-carrier waveform contribute both to the increase in z_{DC} . Transmitting over multiple carriers results in higher ECEs – this benefit is added onto the gains due to optimization of the symbols' p.m.f. relative to the non-optimized QPSK with equiprobable signaling. As such, QPSK with uniform p.m.f. provides a lower bound for harvested energy, which is constant for all values of rate, irrespective of the number of carriers. In general, symmetric MPSK with uniform p.m.f. gives $\xi = 0$, meaning that there is no fourth order contribution in z_{DC} in (19) and the same energy-rate per subband performance is predicted analytically for any N (and M as discussed in Section IV.A). In practice, this is true for any large N (e.g. $N \geq 8$ as observed from Fig. 8) due to random modulations

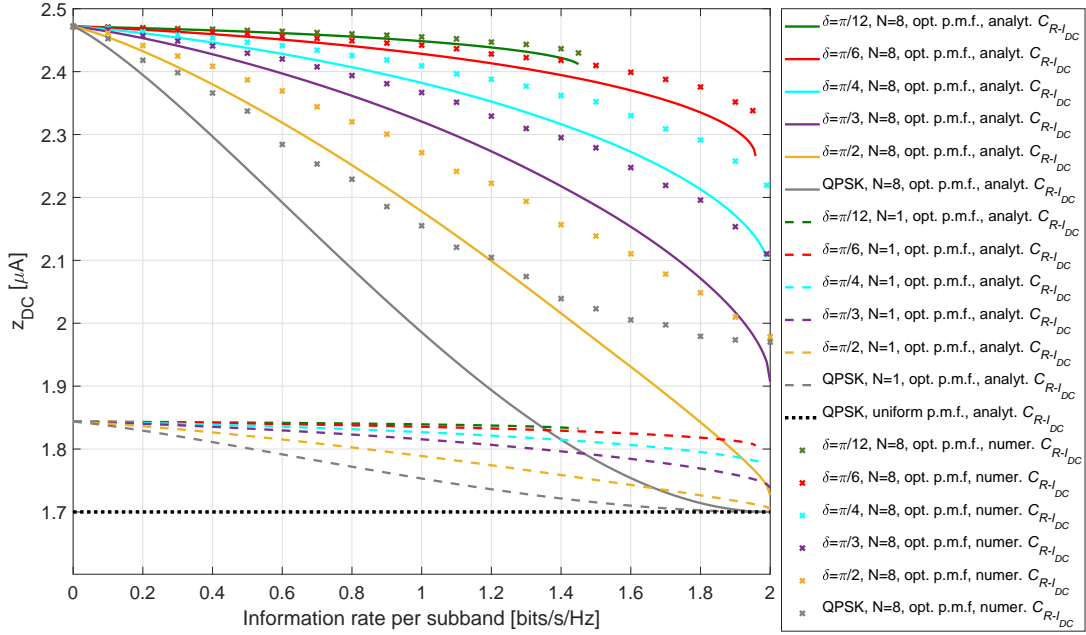


Fig. 10. Analytical C_{R-IDC} for $N = \{1, 8\}$ and numerical C_{R-IDC} for $N = 8$ as a function of δ for asymmetric 4PSK modulation with optimized (opt.) p.m.f. The lower bound for analytical C_{R-IDC} is given by QPSK with uniform p.m.f.

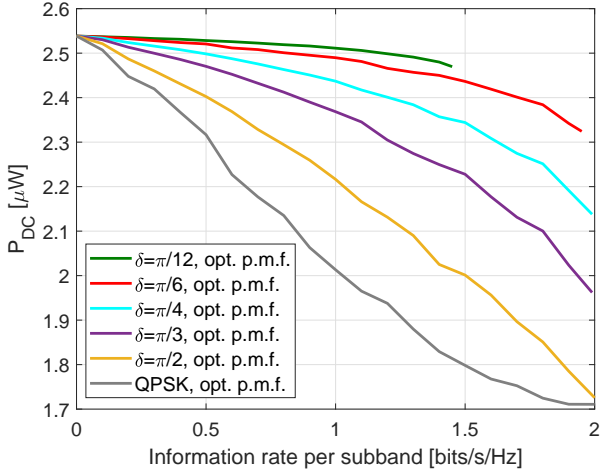


Fig. 11. $R - P_{DC}$ region as a function of δ for $N = 8$ and $M = 4$.

of phase at each carrier resulting in a random aperiodic time-domain waveform with low instantaneous PAPR that is unable to deliver high ECE at the rectifier [23].

It is also noted that it is possible to significantly enlarge the rate-energy region when the phase range of symbols is limited, i.e. M PSK constellation is concentrated in only a fraction of the circle on the complex plane. It is observed that the rate-energy region is maximized most with $\delta = \pi/6$, giving the best value of δ for this setup out of the tested values. It can also be derived analytically that for all values of δ , $\xi = 1$ when only one symbol is transmitted with probability 1 giving the maximum energy point of $z_{DC} = 2.47 \mu A$, with the full details on the resultant p.m.f. given further in Section IV.D. In accordance with Fig. 9, smaller phase ranges with $\delta =$

$\{\pi/12, \pi/6\}$ do not allow to achieve the maximum normalized rate of 2 bits/s/Hz at the SNR of 20dB. The resultant optimized p.m.f. of symbols also converges to that obtained with the Blahut-Arimoto algorithm at maximum rate points.

The simulation-based rate-energy region is also shown in Fig. 10 for $N = 8$, verifying the suitability of the EH z_{DC} model (19) for performing optimization of asymmetric M PSK modulation. In order to obtain the numerical results, z_{DC} was calculated as the time average using (6). The averaging is performed over several hundred symbol periods, with symbols transmitted independently on each carrier and the symbol probabilities optimized for the tested phase ranges and at a given rate requirement. As $N = 8$ used in the comparison of the analytical and the numerical rate-energy regions is rather small, a gap between the regions' boundaries of the order similar to the one in Fig. 7 is observed. This inaccuracy occurs due to the reason mentioned in Section IV.A, whereby for small N , the constructive combining of the carriers with the same phase is not captured by the analytical model (19). Nevertheless, this does not affect the optimization results, as essentially the objective is to maximize the component ξ , which is independent of N , in z_{DC} in (19).

In order to validate the results in Fig. 10, the single series rectifier circuit (Fig. 6) is simulated by reusing the input data signals generated for $N = 8$, with the p.m.f. of 4PSK symbols optimized for a set of δ values. The rate- P_{DC} region graph in Fig. 11 confirms the analytical and the numerical rate- z_{DC} region results in Fig. 10. This validates the EH model and modulation design and highlights the importance of using optimized modulation design in order to increase the ECE of a practical rectenna circuit in the SWIPT configuration.

Finally, the results of the optimization using SQP are compared with the globally optimal solution obtained with

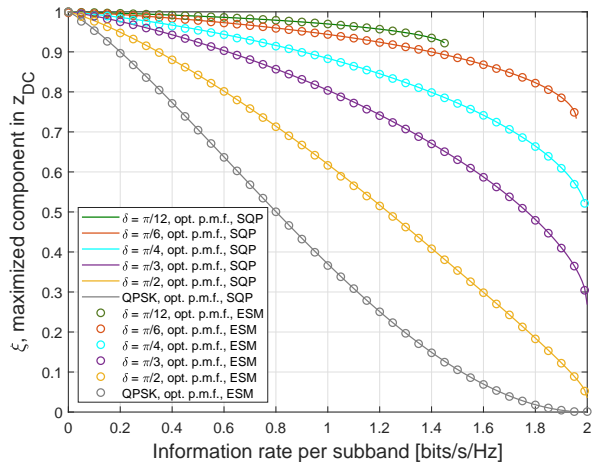


Fig. 12. $R - \xi$ region as a function of δ for $M = 4$, with the optimal p.m.f. obtained with SQP and ESM algorithms.

the exhaustive search method (ESM) in Fig. 12. The rate-energy regions are presented as normalized rate- ξ regions, where ξ is the component in (19) that needs to be maximized for energy transfer. It is noted that the two sets of results match well, verifying the suitability of the SQP algorithm with an appropriate choice of the initialization point to solve the optimization problem (29)-(31) efficiently.

D. Analysis of Optimized Symbols P.M.F.

Fig. 13 shows the resultant p.m.f. of the 4PSK symbols for a set of δ and SNR values. The plot displays locally optimal optimization results. Deriving conditions under which the maximum energy is attainable eliminates the need for the random start during optimization. As $\xi = 1$ is achievable when only one symbol is transmitted, choosing the initial start p.m.f. as, for instance, $[0 \ 1 \ 0 \ 0]$ allows to obtain the rate-energy region boundaries efficiently.

The maximum gain in terms of energy is achievable in the lower rate region when one symbol (e.g. x_1) is allocated dominant probability, with the two closest symbols (x_0 and x_2) getting equal probability ($p_0 = p_2$) to gradually increase the rate, which follows from the expression for Θ (10). Equivalently, other subset of neighbouring symbols could provide the same result. The phase shifts due to the two symbols near the dominant one compensate each other on average. As the rate requirement rises, the full constellation becomes utilized and the optimization pattern changes for the case of the asymmetric 4PSK. The two inner symbols (x_1 and x_2) and the two outer symbols (x_0 and x_3) now get equal probability, i.e. $p_1 = p_2$ and $p_0 = p_3$, and the corresponding plots of the probabilities coincide. For the standard QPSK constellation, the pattern does not change and $p_0 = p_2$ applies for the full range of rate.

For the case of the asymmetric PSK, as the requirement on rate increases and the requirement on energy decreases, the optimization results in the reallocation of probability weights from the inner symbols maximizing energy – to the outer symbols maximizing rate, in accordance with the analysis in

Sections III.B and III.C and the simulation results in Section IV.B. At a relatively high energy point, the inner symbols get allocated most of the probability mass, ≈ 0.45 each. Depending on the SNR and δ , the outer symbols gain more weight as the required rate increases, until the p.m.f. becomes near uniform ($p_m \approx 0.25$) at the maximum rate point at 20dB SNR and at a lower rate point at 10dB SNR. For the higher SNR value, the p.m.f. of the input symbols is close to uniform for all δ values, when the rate is at maximum. For the lower SNR value, the demand on rate results in the probability plot of the outer symbols overshooting the probability plot of the inner symbols, with the overshoot increasing and occurring for lower rate as δ decreases.

The underlying physical process behind the energy maximization is that when carriers carry symbols with relatively small phase differences, the carrier peaks are closer in phase at the receiver giving a larger peak amplitude of the multi-carrier waveform, which in turn is able to produce a higher voltage at the output of the diode-based rectifier, due to its non-linear behaviour. However, with the active rate constraint, this mechanism needs to be balanced with improving the error probability of symbol detection, thereby gradually allocating the outer symbols more probability mass as the rate is increased.

E. Analysis of Rate-Energy Scaling with Modulation Order M

Finally, for every δ the rate-energy region can only be enlarged up to a certain value of M , and increasing M further would not bring any significant benefit at a given SNR. As shown in Fig. 14, the boundaries of the largest regions achievable for every δ can, for example, be reached with conditions ($\delta = \pi/6; M = 8$), ($\delta = \pi/4; M = 16$), ($\delta = \pi/3; M = 16$), ($\delta = \pi/2; M = 32$).

Fig. 15 shows the scaling of z_{DC} with $\log_2(N)$ calculated at minimum energy – maximum rate points, when optimized input symbol distributions turn out to be close to uniform at the SNR of 20dB. It is observed that z_{DC} obtained with the asymmetric MPSK modulation follows the scaling law (14) derived for $\Phi_n \sim U[-\delta, \delta]$, illustrating the analysis in Section III.B, and Fig. 15 can be related to the analytical results in Fig. 7, replotted here (in Fig. 15) for convenience of comparison. It is noted that z_{DC} obtained with the scaling law (14) for the uniformly distributed phase is slightly higher than z_{DC} with the asymmetric MPSK modulation. This difference in plots is attributed to the fact that the optimized symbol probabilities are close to but not exactly uniform, as observed in Fig. 13 and discussed in Section IV.D. It is demonstrated that the scaling law (14) matches the scaling law (19) in case of the uniform p.m.f. of MPSK symbols (that is optimal for different rate-energy points at different SNRs), provided that M is above a certain limit \bar{M} for a given δ . In such case, at high SNR values, the scaling law (14) approximates a lower bound for z_{DC} using asymmetric MPSK modulation for SWIPT.

To summarize, the choice of different parameters of the asymmetric MPSK modulation has an effect on the rate and energy delivered to the SWIPT system using multi-carrier transmission: larger phase range δ increases the information

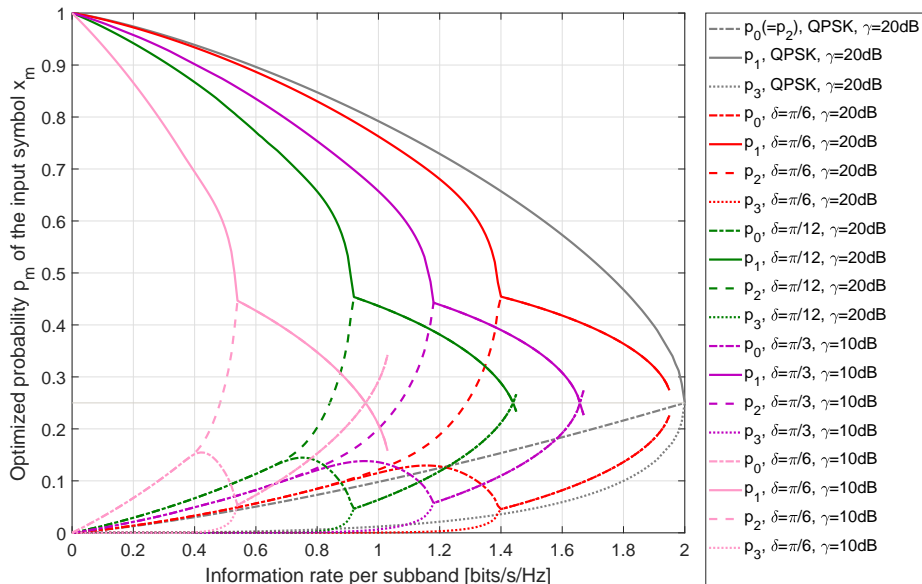


Fig. 13. Optimized probabilities of 4PSK input symbols for $\gamma = \{20, 10\}$ dB and various δ as a function of information rate.

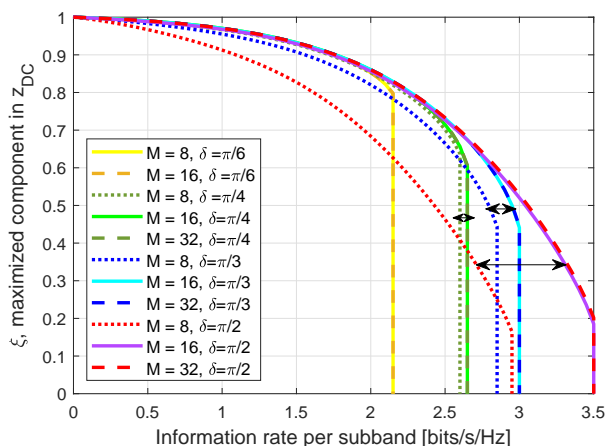


Fig. 14. $R - \xi$ region as a function of M and δ , $\gamma = 20$ dB. The black arrows indicate the gaps between the boundaries of the $R - \xi$ regions for a given δ that can be overcome by increasing M .

rate but decreases the harvested energy; greater modulation order M up to a limit \bar{M} enlarges the whole rate-energy region; and increasing the number of carriers scales up the energy for the same information rate per subband.

V. CONCLUSIONS

In this paper, we proposed the asymmetric PSK modulation, specifically designed for SWIPT. We optimized the probabilities of symbols for the symmetric and the presented asymmetric PSK modulations, thereby enlarging the SWIPT rate-energy region considerably as compared to the equiprobable symmetric PSK. Such modulation design is enabled by using the accurate nonlinear model for the rectifier at the energy harvesting and information decoding receiver. A unified information- and energy-carrying multi-carrier waveform is

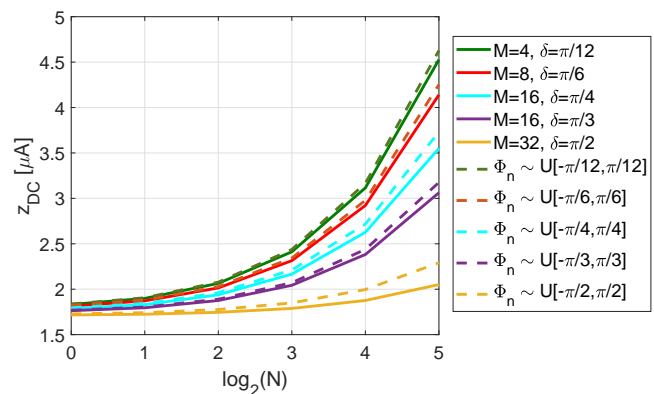


Fig. 15. z_{DC} (solid lines) using asymmetric MPSK modulation, optimized for minimum energy - maximum rate points, $\gamma = 20$ dB, and z_{DC} (dash lines) obtained with the scaling law for the uniformly distributed phase, as a function of $\log_2(N)$.

used for the purpose of SWIPT. The gain in the harvested energy due to using optimized modulation design is additive to the increase in the ECE achieved by utilizing multiple carriers.

The trade-off between harvested energy and information rate manifests itself in the optimization of the input probabilities of the PSK symbols, which are different for the vertices of the rate-energy region, depending on whether maximum rate or energy is achieved, and change in-between. This is due to the conflicting mechanism inherent to SWIPT, whereby WPT requires phases of carriers to be equal, i.e. transmitting only one symbol, whereas WIT aims at maximizing the rate by using the constellation in full, while minimizing the probability of error between symbols.

An interesting extension of this work would be adapting the asymmetric PSK modulation for the frequency-selective

channel. The nonlinear EH model could also be applied in optimizing other practical modulation schemes for SWIPT, by examining not only phase but also amplitude asymmetry of the constellation. Among other open problems for future research, is deriving practical modulation design for power splitting and time switching SWIPT receivers, examining the suitability of asymmetric PSK for backscatter communication, as well as designing error-correcting codes for the new modulation schemes.

APPENDIX A

MAP DETECTOR FOR ASYMMETRIC MPSK MODULATION

Denoting the detected output symbol as \hat{X} and omitting the subchannel index, we derive a decision rule for the MAP detector at the receiver as

$$\hat{X}(y) = \arg \max_{\{x_m\}_{m=0}^{M-1}} p_{Y|X}(y|x_m) \Pr(X = x_m), \quad (35)$$

or equivalently, in terms of phase for the asymmetric MPSK modulation,

$$\hat{X}(\phi) = \arg \max_{\{x_m\}_{m=0}^{M-1}} p_{\Phi|X}(\phi|x_m) \Pr(X = x_m), \quad (36)$$

where $p_{\Phi|X}(\phi|x_m)$ is obtained as in (27).

APPENDIX B

EXAMPLE OF SIGNOMIAL TERM IN z_{DC} FOR MPSK

Consider an example of MPSK modulation with limited phase range and $M = 4$. By calculating the p.m.f. $\bar{\mathbf{p}} = \tilde{\mathbf{p}} * \tilde{\mathbf{p}}$ with $\tilde{\mathbf{p}} \triangleq \mathbf{p} * \tilde{\mathbf{p}}$, corresponding to the random variable Θ , we have

$$\tilde{\mathbf{p}} = [p_0 p_3, (p_0 p_2 + p_1 p_3), (p_0 p_1 + p_1 p_2 + p_2 p_3), (p_0^2 + p_1^2 + p_2^2 + p_3^2), (p_0 p_1 + p_1 p_2 + p_2 p_3), (p_0 p_2 + p_1 p_3), p_0 p_3] \quad (37)$$

and

$$\begin{aligned} \bar{\mathbf{p}} = & [p_0^2, 2\tilde{p}_0\tilde{p}_1, (2\tilde{p}_0\tilde{p}_2 + \tilde{p}_1^2), 2(\tilde{p}_0\tilde{p}_3 + \tilde{p}_1\tilde{p}_2), (2\tilde{p}_0\tilde{p}_4 \\ & + 2\tilde{p}_1\tilde{p}_3 + \tilde{p}_2^2), 2(\tilde{p}_0\tilde{p}_5 + \tilde{p}_1\tilde{p}_4 + \tilde{p}_2\tilde{p}_3), (2\tilde{p}_0\tilde{p}_6 + 2\tilde{p}_1\tilde{p}_5 \\ & + 2\tilde{p}_2\tilde{p}_4 + \tilde{p}_3^2), 2(\tilde{p}_1\tilde{p}_6 + \tilde{p}_2\tilde{p}_5 + \tilde{p}_3\tilde{p}_4), (2\tilde{p}_2\tilde{p}_6 + 2\tilde{p}_3\tilde{p}_5 \\ & + \tilde{p}_4^2), 2(\tilde{p}_3\tilde{p}_6 + \tilde{p}_4\tilde{p}_5), (2\tilde{p}_4\tilde{p}_6 + \tilde{p}_5^2), 2\tilde{p}_5\tilde{p}_6, \tilde{p}_6^2]. \end{aligned} \quad (38)$$

The resultant $\xi = \cos(\theta)\bar{\mathbf{p}}^T$ is in general a signomial in p_m , since some coefficients $\cos(\theta_k) < 0$. For a particular case of $M = 4$, ξ is a posynomial for a small range of phase ($\delta \lesssim \pi/8$).

APPENDIX C

GRADIENTS OF THE ENERGY AND RATE FUNCTIONS

The details of the analytical expressions for gradients $\nabla f_0(\mathbf{p})$ and $\nabla f_1(\mathbf{p})$, as supplied in SQP optimization, are given below.

In order to compute the gradient of the energy function $\nabla f_0(\mathbf{p})$, the partial derivatives $\frac{\partial \xi}{\partial p_m}$ are obtained as

$$\frac{\partial \xi}{\partial p_m} = \cos(\theta) \frac{\partial \bar{\mathbf{p}}^T}{\partial p_m}. \quad (39)$$

The implementation of the gradient of the rate constraint function $\nabla f_1(\mathbf{p})$ relies on taking a double integral over the real and imaginary parts of the received symbol y in order to compute $H(Y)$ numerically. The output entropy $H(Y)$ in (22) is given as

$$\begin{aligned} H(Y) = & - \int_{-\infty}^{\infty} \int_{-\infty}^{\infty} \log_2 \left(\sum_{m=0}^{M-1} \frac{p_m}{\pi} \exp \left(- \left(y_{re} \right. \right. \right. \\ & \left. \left. \left. - \sqrt{\gamma} \cos(\phi_m) \right)^2 - \left(y_{im} - \sqrt{\gamma} \sin(\phi_m) \right)^2 \right) \right) \sum_{m=0}^{M-1} \frac{p_m}{\pi} \exp \left(\right. \\ & \left. \left. - \left(y_{re} - \sqrt{\gamma} \cos(\phi_m) \right)^2 - \left(y_{im} - \sqrt{\gamma} \sin(\phi_m) \right)^2 \right) dy_{re} dy_{im} \end{aligned} \quad (40)$$

and using the theorem of Dominated Convergence, the partial derivatives $\frac{\partial H}{\partial p_m}$ are obtained as

$$\begin{aligned} \frac{\partial H}{\partial p_m} = & - \int_{-\infty}^{\infty} \int_{-\infty}^{\infty} \frac{1}{\pi} \exp \left(- \left(y_{re} - \sqrt{\gamma} \cos(\phi_m) \right)^2 - \left(y_{im} \right. \right. \\ & \left. \left. - \sqrt{\gamma} \sin(\phi_m) \right)^2 \right) \left[\frac{1}{\ln 2} + \log_2 \left(\sum_{m=0}^{M-1} \frac{p_m}{\pi} \exp \left(- \left(y_{re} \right. \right. \right. \right. \right. \\ & \left. \left. \left. - \sqrt{\gamma} \cos(\phi_m) \right)^2 - \left(y_{im} - \sqrt{\gamma} \sin(\phi_m) \right)^2 \right) \right] dy_{re} dy_{im}. \end{aligned} \quad (41)$$

REFERENCES

- [1] E. Bayguzina and B. Clerckx, "Modulation design for wireless information and power transfer with nonlinear energy harvester modeling," in *Proc. IEEE 19th Int. Workshop Signal Process. Adv. Wireless Commun. (SPAWC)*, Jun. 2018.
- [2] B. Clerckx *et al.*, "Fundamentals of wireless information and power transfer: from RF energy harvester models to signal and system designs," *IEEE J. Sel. Areas Commun.*, vol. 37, no. 1, pp. 4–33, Jan. 2019.
- [3] H. J. Visser and R. J. M. Vullers, "RF energy harvesting and transport for wireless sensor network applications: principles and requirements," *Proc. IEEE.*, vol. 101, no. 6, pp. 1410–1423, Jun. 2013.
- [4] M. Pinuela, S. Lucyszyn, and P.D. Mitcheson, "Ambient RF energy harvesting in urban and semi-urban environments," *IEEE Trans. Microwave Theory and Techn.*, vol. 61, no. 7, pp. 2715–2726, Jul. 2013.
- [5] N. Shinohara, "Power without wires," *IEEE Microw. Mag.*, vol. 12, no. 7, pp. S64–S73, Dec. 2011.
- [6] C. R. Valenta and G. D. Durgin, "Harvesting wireless power: Survey of energy-harvester conversion efficiency in far-field, wireless power transfer systems," *IEEE Microw. Mag.*, vol. 15, no. 4, pp. 108–120, Jun. 2014.
- [7] B. Clerckx, A. Costanzo, A. Georgiadis, and N. B. Carvalho, "Toward 1G mobile power networks: RF, signal, and system designs to make smart objects autonomous," *IEEE Microw. Mag.*, vol. 19, no. 6, pp. 69–82, Sep./Oct. 2018.
- [8] U. Madhow, *Fundamentals of Digital Communication*, New York: Cambridge University Press, 2008.
- [9] H. Sakaki, S. Yoshida, K. Nishikawa, and S. Kawasaki, "Analysis of rectifier operation with FSK modulated input signal," in *Proc. IEEE Wireless Power Transfer Conf. (WPTC)*, May 2013, pp. 187–190.
- [10] H. Sakaki *et al.*, "Analysis of rectifier RF-DC power conversion behavior with QPSK and 16QAM input signals with WiCoPt system," in *Proc. Asia-Pacific Microw. Conf. (APMC)*, Nov. 2014, pp. 603–605.
- [11] H. Sakaki, K. Nishikawa, S. Yoshida, and S. Kawasaki, "Modulated scheme and input power impact on rectifier RF-DC Efficiency for WiCoPt system," in *Proc. 45th European Microw. Conf. (EuMC)*, Sept. 2015, pp. 60–63.
- [12] F. Bolos, J. Blanco, A. Collado, and A. Georgiadis, "RF energy harvesting from multi-tone and digitally modulated signals," *IEEE Trans. Microw. Theory Techn.*, vol. 64, no. 6, pp. 1918–1927, Jun. 2016.

- [13] D. I. Kim, J. H. Moon, and J. J. Park, "New SWIPT using PAPR: How It works," *IEEE Wireless Commun. Lett.*, vol. 5, no. 6, pp. 672–675, Dec. 2016.
- [14] S. Claessens *et al.*, "Enhanced biased ASK modulation performance for SWIPT with AWGN channel and dual-purpose hardware," *IEEE Trans. Microw. Theory Techn.*, vol. 66, no. 7, pp. 3478–3486, Jul. 2018.
- [15] T. A. Zewde and M. C. Gursoy, "Simultaneous wireless information and power transfer with finite-alphabet input signals," in *Proc. IEEE 82nd Vehicular Technology Conference (VTC2015-Fall)*, Sept. 2015, pp. 1–5.
- [16] I. M. Kim and D. I. Kim, "Wireless information and power transfer: rate-energy tradeoff for equi-probable arbitrary shaped discrete inputs," *IEEE Trans. Wireless Commun.*, vol. 15, no. 6, pp. 4393–4407, Jun. 2016.
- [17] R. Zhang and C. K. Ho, "MIMO broadcasting for simultaneous wireless information and power transfer," *IEEE Trans. Wireless Commun.*, vol. 12, no. 5, pp. 1989–2001, May 2013.
- [18] J. Park and B. Clerckx, "Joint wireless information and energy transfer in a two-user MIMO interference channel," *IEEE Trans. Wireless Commun.*, vol. 12, no. 8, pp. 4210–4221, Aug. 2013.
- [19] K. Huang and E. G. Larsson, "Simultaneous information and power transfer for broadband downlink systems," *IEEE Trans. Signal Process.*, vol. 61, no. 23, pp. 5972–5986, Dec. 2013.
- [20] W. Liu, X. Zhou, S. Durrani, and P. Popovski, "SWIPT with practical modulation and RF energy harvesting sensitivity," in *Proc. IEEE Int. Conf. Commun. (ICC)*, May 2016, pp. 1–7.
- [21] R. Rajashekar *et al.*, "A finite input alphabet perspective on the rate-energy tradeoff in SWIPT over parallel Gaussian channels," *IEEE J. Sel. Areas Commun.*, vol. 37, no. 1, pp. 48–60, Jan. 2019.
- [22] B. Clerckx and E. Bayguzina, "Waveform design for wireless power transfer," *IEEE Trans. Signal Process.*, vol. 64, no. 23, pp. 6313–6328, Dec. 2016.
- [23] B. Clerckx, "Wireless information and power transfer: nonlinearity, waveform design and rate-energy tradeoff," *IEEE Trans. Signal Process.*, vol. 66, no. 4, pp. 847–862, Feb. 2018.
- [24] E. Boshkovska *et al.*, "Robust resource allocation for MIMO wireless powered communication networks based on a non-linear EH model," *IEEE Trans. Commun.*, vol. 65, no. 5, pp. 1984–1999, May 2017.
- [25] X. Xu, A. Özçelikkale, T. McKelvey, and M. Viberg, "Simultaneous information and power transfer under a non-linear RF energy harvesting model," in *Proc. IEEE Int. Conf. Commun. Workshops (ICC Workshops)*, May 2017, pp. 179–184.
- [26] K. Xiong, B. Wang, and K. J. R. Liu, "Rate-energy region of SWIPT for MIMO broadcasting under nonlinear energy harvesting model," *IEEE Trans. Wireless Commun.*, vol. 16, no. 8, pp. 5147–5161, Aug. 2017.
- [27] J.-M. Kang, I.-M. Kim, and D. I. Kim, "Wireless information and power transfer: Rate-energy tradeoff for nonlinear energy harvesting," *IEEE Trans. Wireless Commun.*, vol. 17, no. 3, pp. 1966–1981, Mar. 2018.
- [28] P. N. Alevizos and A. Bletsas, "Sensitive and nonlinear far-field RF energy harvesting in wireless communications," *IEEE Trans. Wireless Commun.*, vol. 17, no. 6, pp. 3670–3685, Jun. 2018.
- [29] B. Clerckx and E. Bayguzina, "A low-complexity adaptive multisine waveform design for wireless power transfer," *IEEE Antennas Wireless Propag. Letters*, vol. 16, pp. 2207–2210, 2017.
- [30] B. Clerckx and J. Kim, "On the beneficial roles of fading and transmit diversity in wireless power transfer with nonlinear energy harvesting," *IEEE Trans. Wireless Commun.*, vol. 17, no. 11, pp. 7731–7743, Nov. 2018.
- [31] J. Kim, B. Clerckx, and P. D. Mitcheson, "Prototyping and experimentation of a closed-loop wireless power transmission with channel acquisition and waveform optimization," in *Proc. IEEE Wireless Power Transfer Conf. (WPTC)*, May 2017.
- [32] Y. Huang and B. Clerckx, "Large-scale multiantenna multisine wireless power transfer," *IEEE Trans. Signal Process.*, vol. 65, no. 21, pp. 5812–5827, Nov. 2017.
- [33] M. Varasteh, B. Rassouli, and B. Clerckx, "Wireless information and power transfer over an AWGN channel: nonlinearity and asymmetric Gaussian signaling," in *Proc. IEEE Inf. Theory Workshop (ITW)*, Nov. 2017, pp. 181–185.
- [34] M. Varasteh, B. Rassouli, and B. Clerckx, "On capacity-achieving distributions for complex AWGN channels under nonlinear power constraints and their applications to SWIPT," arXiv:1712.01226, 2017.
- [35] A. S. Boaventura and N. B. Carvalho, "Maximizing DC power in energy harvesting circuits using multisine excitation," in *IEEE MTT-S Int. Microwave Symp. Dig. (MTT)*, Jun. 2011, pp. 1–4.
- [36] F. Killmann and E. von Collani, "A note on the convolution of the uniform and related distributions and their use in quality control," *Economic Quality Control*, vol. 16, no. 1, pp. 17–41, 2001.
- [37] C. Boyer and S. Roy, "Coded QAM backscatter modulation for RFID," *IEEE Trans. Commun.*, vol. 60, no. 7, pp. 1925–1934, Jul. 2012.
- [38] F. Hesar and S. Roy, "Minimum energy source coding for asymmetric modulation with application to RFID," in *Proc. IEEE Int. Conf. RFID (RFID)*, Apr.-May 2013, pp. 207–214.
- [39] C. Boyer and S. Roy, "Backscatter communication and RFID: coding, energy, and MIMO analysis," *IEEE Trans. Commun.*, vol. 62, no. 3, pp. 770–785, Mar. 2014.
- [40] M. C. Gursoy, "On the low-SNR capacity of phase-shift keying with hard-decision detection," in *Proc. Int. Symp. Inf. Theory (ISIT)*, Jun. 2007, pp. 166–170.
- [41] S. Arimoto, "An algorithm for calculating the capacity of an arbitrary discrete memoryless channel," *IEEE Trans. Inf. Theory*, vol. 18, pp. 14–20, 1972.
- [42] R. E. Blahut, "Computation of channel capacity and rate distortion functions," *IEEE Trans. Inf. Theory*, vol. 18, pp. 460–473, 1972.
- [43] M. Chiang, "Geometric programming for communication systems," *Found. Trends Commun. Inf. Theory*, vol. 2, no. 1/2, pp. 1–154, Aug. 2005.
- [44] P. T. Boggs and J. W. Tolle, "Sequential Quadratic Programming," *Acta Numerica*, vol. 4, pp. 1–51, 1995.